A laboratory model of Saturn's North Polar Hexagon

Ana C. Barbosa Aguiar *, Peter L. Read, Robin D. Wordsworth, Tara Salter, Y. Hiro Yamazaki

Atmospheric, Oceanic and Planetary Physics, Department of Physics, University of Oxford, Clarendon Laboratory, Parks Road, Oxford OX1 3PU, UK

ARTICLE INFO

ABSTRACT

A hexagonal structure has been observed at ∼76°N on Saturn since the 1980s (Godfrey, D.A. [1988]. Icarus 76, 335–356). Recent images by Cassini (Baines, K., Momary, T., Roos-Serote, M., Atreya, S., Brown, R., Buratti, B., Clark, R., Nicholson, P. [2007]. Geophys. Res. Abstr. 9, 02109; Baines, K., Momary, T., Fletcher, L., Kim, J., Showman, A., Atreya, S., Brown, R., Buratti, B., Clark, R., Nicholson, P. [2009]. Geophys. Res. Abstr. 11, 3375) have shown that the feature is still visible and largely unchanged. Its long lifespan and geometry has puzzled the planetary physics community for many years and its origin remains unclear. The measured rotation rate of the hexagon may be very close to that of the interior of the planet (Godfrey, D.A. [1990]. Science 247, 1206–1208; Caldwell, J., Hua, X., Turgeon, B., Westphal, J.A., Barnet, C.D. [1993]. Science 206, 326–329; Sánchez-Lavega, A., Lecacheux, J., Colas, F., Laques, P. [1993]. Science 260, 329–332), leading to earlier interpretations of the pattern as a stationary planetary wave, continuously forced by a nearby vortex (Allison, M., Godfrey, D.A., Beebe, R.F. [1990]. Science 247, 1061–1063). Here we present an alternative explanation, based on an analysis of both spacecraft observations of Saturn and observations from laboratory experiments where the instability of quasi-geostrophic barotropic (vertically uniform) jets and shear layers is studied. We also present results from a barotropic linear instability analysis of the saturnian zonal wind profile, which are consistent with the presence of the hexagon in the North Pole and absence of its counter-part in the South Pole. We propose that Saturn's long-lived polygonal structures correspond to wavemodes caused by the nonlinear equilibration of barotropically unstable zonal jets.

© 2009 Elsevier Inc. All rights reserved.

1. Introduction

Saturn's hexagon was first noted in images taken by the Voyager spacecraft (Godfrey, 1988), but it has also been studied more recently using the Hubble Space Telescope (Caldwell et al., 1993) and by the Cassini mission (Baines et al., 2007, 2009; Fletcher et al., 2008), which has allowed for observations of the northern hemisphere during different seasons. The persistence of the feature over several decades indicates that it is not sensitive to seasonal variations of solar forcing (Sánchez-Lavega et al., 1993). A prominent vortex was noted on one side of the hexagon by Godfrey at the time of the Voyager encounter, although a two-dimensional velocity field (produced by cloud tracking) also suggested the possible existence of a further five weak anticyclonic vortices, located adjacent to the outer edge of each side of the polygonal-shaped jet (Godfrey, 1988). In the latest images from Cassini (Baines et al., 2009), a few of these vortices can occasionally be seen.

The observation of this highly symmetric, geometrical feature on Saturn has led to much speculation concerning its nature and origin. One notable suggestion that has been widely cited is that it is a Rossby wave train that is *stationary* in the planet's rotating frame, nested in an eastward jet that is perturbed by a large *solitary vortex* observed during the Voyager encounter (Allison et al., 1990), the origin of which is unexplained. However, this theory relies on two assumptions that are only weakly supported by observational evidence, namely, that the hexagon is rigidly fixed in the frame of Saturn's interior (Godfrey, 1990; Read et al., 2009a), and that the solitary forcing vortex is a permanent feature. Two different measurements of the drift speed of the most prominent visible vortex, suggested to force the hexagon, have indicated that the spots visible on each occasion may actually be different features (Sánchez-Lavega et al., 1993). Also, the interior rotation rate of Saturn is not accurately known (Baines et al., 2007; Gurnett et al., 2005), and thus the drift speed of both the hexagon and the prominent vortex with respect to the planetary interior remain uncertain. Most recently, observations from Cassini VIMS (Baines et al., 2007) and CIRS (Fletcher et al., 2008) indicate that the hexagon penetrates deeply into the troposphere to at least the 2–4 bar level, but does not extend into the stratosphere. Moreover, there is now no evidence for the prominent solitary vortex found by Voyager. There remain, therefore, a number of uncertainties and the phenomenon is as yet poorly understood.

* Corresponding author. Present Address: Instituto de Oceanografia, Faculdade de Ciências da Universidade de Lisboa, 1749-016 Campo Grande, Lisboa, Portugal.
E-mail address: aaaguiar@fc.ul.pt (A.C. Barbosa Aguiar).

In this paper, we consider the possibility that the hexagon forms as the result of the nonlinear development of a predominantly barotropic instability of the strong eastward zonal jet at 77.5°N on Saturn. Numerous studies have remarked upon the tendency of many of the zonal jet-like structures on both Jupiter and Saturn to violate the classical Rayleigh–Kuo criterion for barotropic stability (Ingersoll et al., 1981, 2004; Limaye, 1986; Sánchez-Lavega et al., 2000). While the violation of this criterion is a necessary condition for barotropic instability, it is not sufficient in itself to guarantee instability (e.g. Dowling, 1995). In Section 2, therefore, we present results from a linear instability analysis of the North Polar Jet on Saturn, which indicates that the jet is expected to be unstable to wave-like disturbances with most unstable zonal wavenumbers $m = 6$–12, within the (limited) applicability of linear instability theory.

In Sections 3–4 we consider a laboratory analogue of the flows on Saturn in which a barotropically unstable jet or shear layer is investigated experimentally to explore the range of possible equilibrated flows in fully developed, highly nonlinear barotropic instability. Although precise dynamical similarity with the features on Saturn is not feasible in every respect, the instability of a jet-like flow on a topographic β-plane forms a close analogue with planetary flows, and leads to a range of equilibrated polygonal waves (including hexagons) under conditions plausibly similar to those on Saturn, at least in terms of Rossby number. These results are discussed in Section 5, both in terms of their comparison with other laboratory studies that have produced polygonal structures in the past, and concerning their possible implications for Saturn and the other gas giant planets.

2. Vorticity structure and stability of Saturn's North Polar Jet

The pattern of zonal jets on Saturn largely consists of alternating eastward and westward jets in each hemisphere, with a meridional separation and wind strength that largely tends to decrease towards the poles. It has been remarked by a number of authors that many of these jets are sufficiently narrow and intense that the northward gradient of absolute vorticity (including the planetary vorticity gradient) actually changes sign, especially in the flanks of the eastward jets. Fig. 1a shows a profile of the zonal wind between 30°N and the North Pole, derived from tracking cloud features in Voyager images by Sánchez-Lavega et al. (2000). Prominent eastward jets are located at planetographic latitudes of around 47°, 60°, 65° and 77.5°N, with the most northerly jet being also the narrowest. Fig. 1b shows the corresponding profile of northward vorticity gradient (solid line) and $df/dy = \beta(y)$ (dashed line). The vorticity gradient profile clearly crosses $\beta(y)$ in several places, robustly confirming that $\beta - u_{yy}$ changes sign.

In general, if a barotropic rotating fluid system is subject to differential rotation in the horizontal, the originally zonally-symmetric flow may become *barotropically unstable*. Depending on the strength of the imposed lateral shear, an instability may develop forming a wave-like disturbance through which the initial jet flow undulates, with the eddies gaining kinetic energy directly at the expense of the kinetic energy of the original zonal flow. A necessary (though not sufficient) condition for barotropic instability is the *Rayleigh–Kuo criterion*, which states that $\partial \bar{q}/\partial y$ (the gradient of total absolute vorticity, $\bar{q} = f - \partial \bar{u}/\partial y$) changes sign within the domain of interest

$$\frac{\partial \bar{q}}{\partial y} = \beta - \frac{\partial^2 \bar{u}}{\partial y^2} < 0, \tag{1}$$

where y is the northward coordinate, $\bar{u}$ is the zonal flow and β is the planetary vorticity gradient, i.e., the rate of change of Coriolis parameter with latitude that occurs in a spherical planetary atmosphere (Pedlosky, 1987).
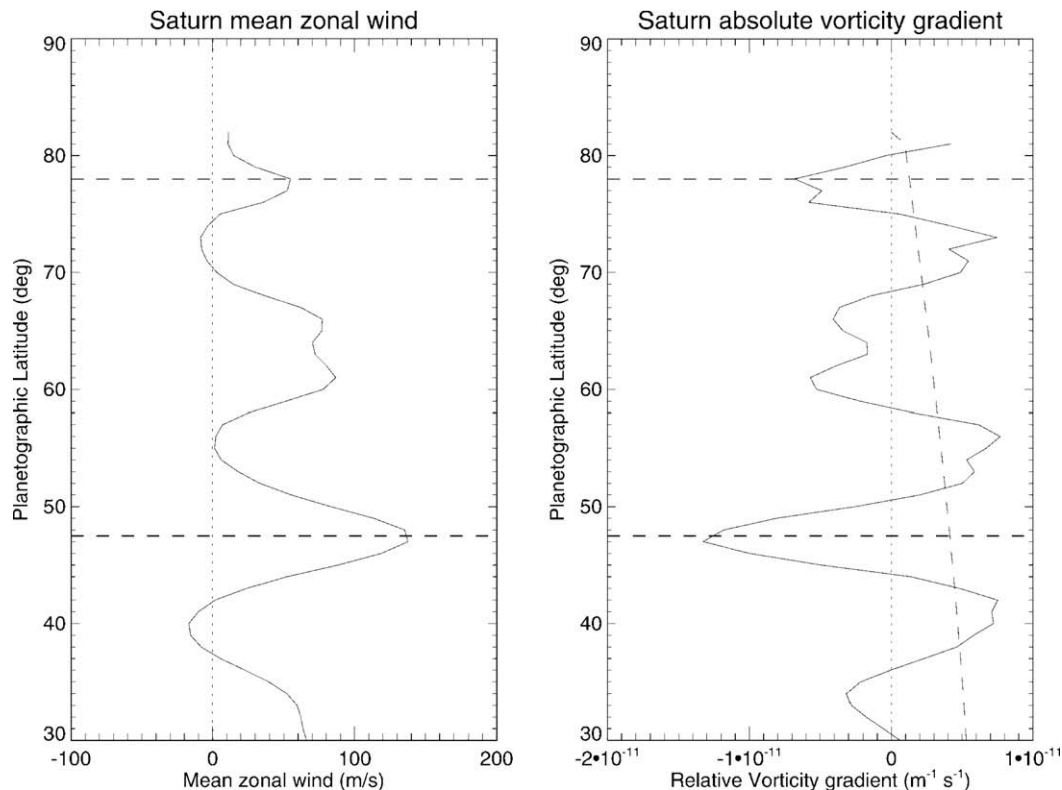

Fig. 1. Profiles measured from Voyager cloud tracking measurements for Saturn's northern hemisphere (Godfrey, 1988), representing the mean zonal winds (a) and associated gradient of vorticity (b). Zonal velocities are measured relative to Voyager's System III. The dotted line on the right represents the planetary vorticity gradient β, indicating violation of the barotropic stability criterion wherever it crosses the solid line. Horizontal dashed lines indicate the hexagon and Ribbon Wave latitudes. For comparison, see the experimental profiles shown in Fig. 6.

Violation of this criterion for barotropic stability is clearly verified (see Fig. 1b) on either side of the jet detected at 77.5°N, and also at the latitude of the Ribbon Wave (47°N; Godfrey, 1988; Sromovsky et al., 1983). This might suggest, therefore, that both features could originate from the barotropic instability of their respective parent zonal jet streams. But simply violating the Rayleigh–Kuo stability criterion is not sufficient by itself to guarantee that instability will take place.

To investigate the stability of the eastward jet at 77.5°N, we have conducted a linear stability analysis of the flow, on the assumption that it is either pure or equivalent-barotropic (with internal deformation radius L_D). The corresponding linearised barotropic vorticity equation for inviscid flow is

$$\frac{\partial q'}{\partial t} + \bar{u}(y)\frac{\partial q'}{\partial x} + \gamma v' = 0, \tag{2}$$

where $\gamma = \overline{\partial q}/\partial y$, $v' = \partial \psi'/\partial x$ is the northward geostrophic eddy velocity and

$$q' = \frac{\partial^2 \psi'}{\partial x^2} + \frac{\partial^2 \psi'}{\partial y^2} - \frac{\pi^2}{L_D^2}\psi' \tag{3}$$

is the eddy vorticity, presented in terms of the geostrophic eddy streamfunction ψ', including a term representing the equivalent-barotropic nature of the flow with finite Rossby deformation radius L_D. The North Polar Jet on Saturn is sufficiently narrow that we can make use of the classical β-plane approximation, and for simplicity we assume that $\partial \psi'/\partial z = 0$ at the upper and lower boundaries. We seek normal mode solutions of the form

$$\psi' = \Psi(y)e^{i(\sigma t - k_0 x)}, \tag{4}$$

leading to the algebraic equation

$$i\sigma D\Psi - ik_0(\bar{u}D + \gamma)\Psi = 0, \tag{5}$$

with $D = \partial_{yy} - k_0^2 - \pi^2/L_D^2$ and $k_0 = m/(r_S \cos \phi_0)$, where r_S is the radius of Saturn and ϕ_0 is the central latitude of the jet. This yields an eigenvalue equation for the phase speed c of the form

$$\left(\frac{\sigma}{k_0}\right)\Psi = c\Psi = D^{-1}(\bar{u}D + \gamma)\Psi. \tag{6}$$

This was solved using standard methods (verified against the classical problem discussed by Pedlosky (1987)) for a zonal velocity profile taken from the measurements of Sánchez-Lavega et al. (2000). The results of this eigenvalue analysis are shown in Fig. 2, which illustrates growth rate curves with zonal wavenumber for a series of cases with values of L_D ranging from 2500 km to ∞ (pure barotropic flow). For pure barotropic flow, the instability analysis suggests a wavenumber of maximum growth rate of around $m_{max} = 13$, with an e-folding timescale $T \sim 12$ saturnian sols. With finite values of L_D, the wavenumber of maximum growth rate and the peak growth rate itself tend to decrease until, for
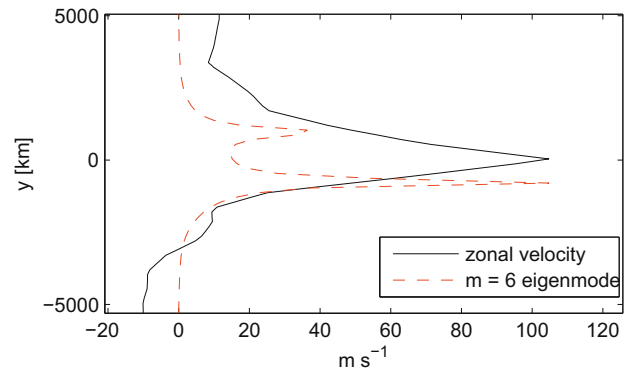
Fig. 3. Normalised profile of the amplitude of the complex streamfunction (as defined in Eq. (6)) with $L_D = 2500$ km for the most rapidly growing $m = 6$ eigenmode (dashed line), together with the latitudinal profile of zonal velocity (black line) at high northern latitudes on Saturn.

$L_D = 2500$ km, $m_{max} \sim 5$–6 and $T \sim 100$ sols. For $L_D = 2000$ km or less, the large-scale instability appears to be suppressed, and the growth rate simply increases monotonically with wavenumber.

For $L_D = 2500$ km, the speed of eigenmode $m = 6$ is near that of the zonal wind at the hexagon's latitude, hence its phase speed *relative to the jet* is approximately zero. The position of the peak of the fastest growing mode relative to the jet (see Fig. 3) coincides with the hexagon position relative to the jet as observed by Godfrey (1988) – see Fig. 1a.

For the polar jet in the southern hemisphere (at 73°S), this stability analysis predicts a growth rate that does not peak at finite wavenumbers and is weaker than that shown in Fig. 2, which seems consistent with the absence of a North Polar Hexagon counter-part in the South Pole.

The fact that the flow is unstable according to linear barotropic theory around the latitudes of the North Polar Hexagon indicates that this process might underlie the origin of the hexagon. The formation and selection of a stable, large-amplitude wave pattern, similar to the one observed by Voyager, HST and Cassini, however, needs further justification that takes fuller account of the nonlinear dynamics of the flow. This can be tackled in various ways. In the following sections, we investigate a possible analogue of the saturnian North Polar Jet in the laboratory. Such a fluid system involves no *ad hoc* approximations and allows us to study the fully developed forms of barotropic instabilities without restriction on wave amplitudes.

3. Laboratory analogue

In fluid-dynamical laboratory studies of various kinds of instability, patterns of waves or chains of vortices aligned in polygonal patterns are commonly found, regardless of the axisymmetric geometry used for the container. These can arise, for example, from a small differential rotation imposed on an already rotating fluid (Hide and Titman, 1967; Konijnenberg et al., 1999; Früh and Read, 1999; Hollerbach et al., 2004; Schaeffer and Cardin, 2005), or by vigorous turning of the upper or lower boundary of the container (Jansson et al., 2006). Similar polygonal patterns have also been observed in satellite images of the eyes of intense terrestrial hurricanes and tropical cyclones (Kossin and Schubert, 2004; Limaye et al., 2009).

Where the pattern extends completely around the experiment in a zonally periodic domain, this may form a regular, stable polygon and associated train of vortices. The zonal wavenumber or number of vortices observed depends on the wavelength that is most energetically favoured, which in turn depends on flow
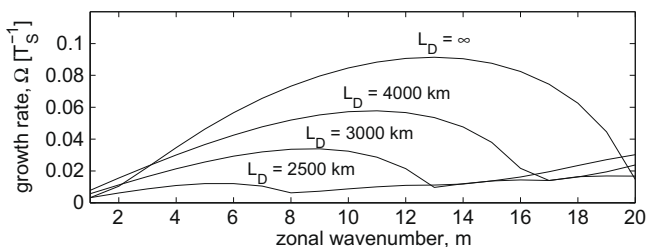

Fig. 2. Growth rate curves as a function of zonal wavenumber for barotropic instabilities of the North Polar Jet on Saturn at 77.5°N, obtained from an eigenvalue analysis (see text) of the observed zonal jet profile. The lines represent the growth rates for different values of the deformation radius L_D.

parameters that take into account the strength of forcing as well as other geometric and dynamical factors of the system. Although the flow becomes non-axisymmetric during the instability, it typically remains vertically uniform so that both the polygon and vortices extend throughout the whole depth of the system, with coherence along a direction parallel to the axis of rotation and no phase tilt with height.

In the experiments presented here, a cylindrical container of diameter 60 cm was filled with fluid and placed on a rotating table coaxially with the axis of rotation. In order to force a flow with a jet-like profile, a differentially-rotating, narrow ring section of outer radius $R = 15$ cm and radial thickness $s = 2$ cm was placed in contact with the upper surface only of the fluid (cf. Niino and Misawa (1984), who used a similar ring in the bottom of a similar tank). The differential rotation was typically small compared to the system's background rotation. This allows for a dominant balance between the horizontal pressure gradient and Coriolis forces, such that *quasi-geostrophy* applies (Pedlosky, 1987). The cylindrical tank was rotated at an angular velocity Ω about a vertical axis of symmetry, while the ring rotated at angular velocity ω (see Figs. 4a and 5). A rigid outer annular section was placed in the tank flush with the ring at the top surface, while the bottom of the tank was either flat or had a conical slope (see Fig. 4a) such that the depth of the tank H increased linearly with radius. A conical bottom could be used to reproduce a topographic beta effect β of magnitude given by

$$\beta = \frac{2\overline{\Omega}}{H_R} \tan \theta, \tag{7}$$

where $\theta \approx 5°$ is the slope angle of the bottom with respect to the horizontal, $H_R = 8.5$ cm was the depth of fluid at the shear layer radius and $\overline{\Omega} = \Omega + \Delta\Omega$ is the mean rotation rate of the fluid in the jet with $\Delta\Omega \approx \omega/4$, assuming that roughly half of the top surface (1/4 of the flat boundaries surface) is differentially-rotating. When using a flat bottom surface, so that $\beta = 0$, $H = H_R = 10.0$ cm. The differentially-rotating ring produced an azimuthal jet-like flow bounded
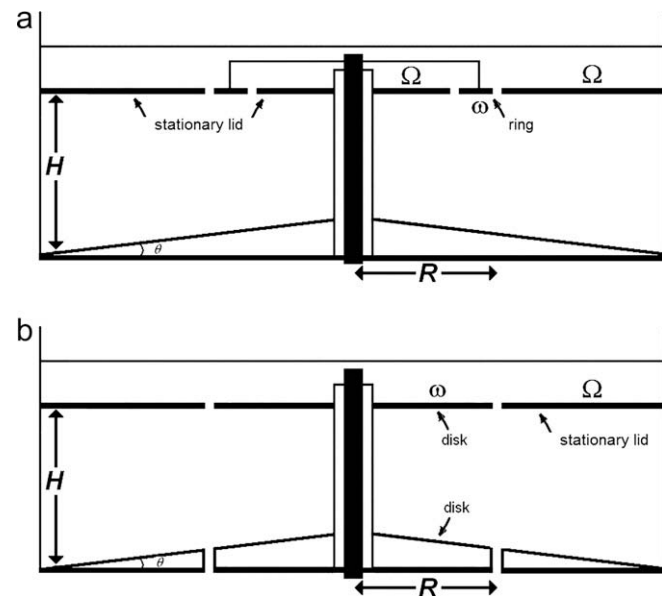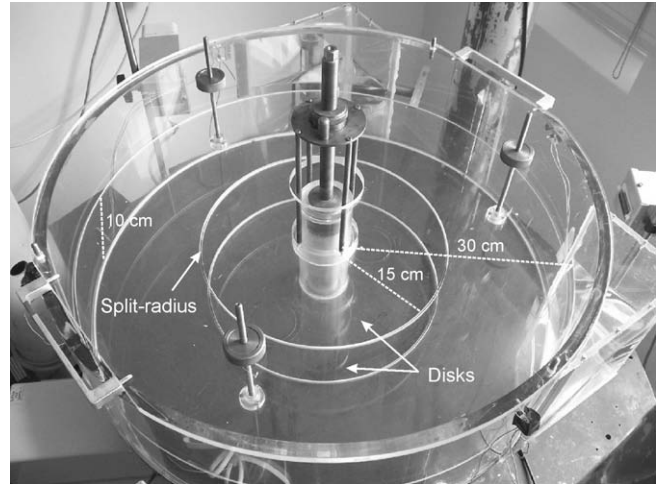

Fig. 5. View of the perspex cylindrical tank with no working fluid. Our experiments were executed in a cylindrical annulus with inner radius $r_i = 3$ cm and outer radius $r_o = 30$ cm, which rotated at angular velocity Ω (up to 4 rad s^{-1}) about a vertical axis of symmetry. The inner axis can rotate freely at angular velocity ω (up to 1.5 rad s^{-1}), driving either two concentric horizontal disks sections of radius $R = 15$ cm at heights $z = 0$ cm and $z = 10$ cm (as in the photograph here and in Fig. 4b), or just a narrow ring section of outer radius $R = 15$ cm and radial thickness $s = 2$ cm at $z = 10$ cm (see Fig. 4a). Rigid, outer annular lids are placed in the tank at heights flush with the inner disks or with the ring.

by two vertically-aligned Stewartson-type shear layers on either side of the jet.

In such conditions, the flow can be characterised by two main dimensionless parameters: the Rossby number, Ro, that gives a measure of the strength of the differential rotation compared to the Coriolis forces, and the Ekman number, E, which is a measure of the viscous dissipation compared to Coriolis forces, where

$$Ro = \frac{R\omega}{2\overline{\Omega}H_R}; \quad E = \frac{\nu}{\overline{\Omega}H_R^2}. \tag{8}$$

For qualitative flow visualisation, we used water as the working fluid and fluorescein dye was injected at one or more points at $r = R$ located at the bottom end wall. For quantitative flow measurements, the fluid used was a mixture of water and glycerol with a density $\rho = 1.045 \pm 0.002 \times 10^3$ kg m^{-3} and kinematic viscosity $\nu = 1.9 \pm 0.1 \times 10^{-6}$ m^2 s^{-1}, which was seeded with neutrally buoyant, white Pliolite tracer particles of diameter 355–500 μm, illuminated by a thin horizontal light sheet. The flow was recorded by a video camera placed coaxially in the frame of the rotating table (rotating at angular velocity Ω), viewing the tank from above. Flow fields were obtained from pairs of images separated by short intervals in time using Correlation Imaging Velocimetry (CIV, Fincham and Spedding, 1997).

4. Experimental results

The results presented in Figs. 6–10 correspond to examples of fully developed $m = 6$ barotropically unstable wave patterns obtained in experiments with constant forcing (Ro, E). Measurements were typically taken over approximately 30 min (over 400–500 tank revolutions) when the flow had reached a steady state. Fig. 6 shows the time and azimuthal mean flow from a typical $m = 6$ pattern at (Ro, E) = (0.074, 7 × 10^{-5}), showing radial profiles of (a) the azimuthal velocity and (b) the radial gradient of relative vorticity at approximately the middle of the tank. This profile is typical of the flow at all heights, which was virtually independent of height except close to the Ekman layers adjacent to the horizontal boundaries, of characteristic thickness $\sim (\nu/\Omega)^{1/2} \sim 1$ mm. The

Fig. 4. Schematic cross-sections of the two laboratory apparatus used: (a) the differentially-rotating ring that drives the barotropic jet is represented by the narrow horizontal section detached from the rest of the lid that is fixed and (b) the differentially-rotating disks are represented by the inner sections at the top and bottom of the tank. In both cases is represented the removable conical slope, with $\theta \approx 5°$.
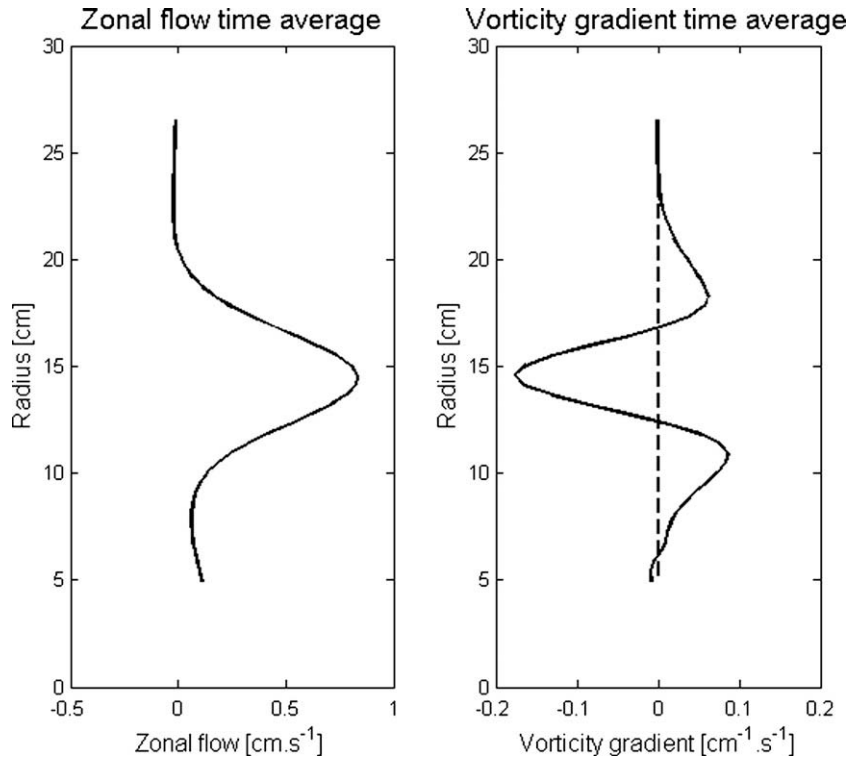
Fig. 6. Azimuthal mean zonal flow (a) and vorticity gradient (b) profiles measured in a frame rotating at Ω in the ring experiment (see Fig. 4a). These correspond to the time-averaged profiles from a sequence of approximately 400 velocity fields obtained by analysis of flow images captured over approximately 30 min (approximately 500 tank days), for $Ro = 7.4 \times 10^{-2}$, $E = 7 \times 10^{-5}$ and $\beta = 0$. A barotropic jet is produced that is quantitatively similar to that observed in each of the saturnian jets (see Fig. 1).
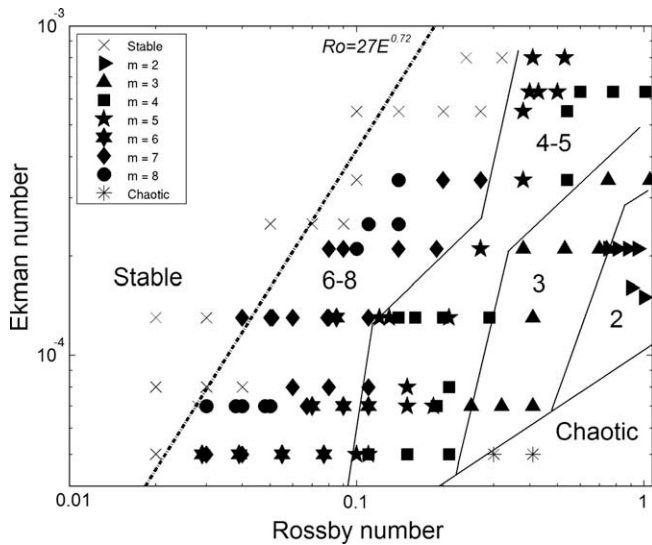

Fig. 7. Regime diagram showing the observed wavenumbers m of barotropic instability found in the barotropic jet experiment as a function of Ro and E when $\beta = 0$, i.e. without the conical slope (see Fig. 4a). The symbols show individual experimental observations and the numbers indicate the regions dominated by each zonal wavenumber. The wavenumber tends to decrease as Ro is increased, but the flow is only weakly dependent on E. Wavemode 6 can be observed for flow parameters $3 \times 10^{-2} \leqslant Ro \leqslant 1 \times 10^{-1}$ and $5 \times 10^{-5} \leqslant E < 2 \times 10^{-4}$. The dashed-dotted line corresponds to Eq. (9) and is drawn here for reference.

vorticity gradient profile shows a strongly negative minimum at the centre of the jet with two weaker positive maxima in the shear layers on either side. These profiles can be compared with those for Saturn's North Polar Jet in Fig. 1, which shows qualitatively very similar structures between latitudes of 72° and 82°N.

4.1. Flow regimes and wavenumber selection

The wavenumber observed, and the overall flow behaviour, depended quite sensitively on the experimental parameters. This was mainly determined by the Rossby number, Ro but with some dependence also on E. A regime diagram was produced by varying the Rossby number in small steps every 15 min or so, while keeping the Ekman number constant for a particular sequence of experiments. By this means, an extensive range of the two-dimensional (Ro, E) parameter space could be efficiently explored, and the main results for the jet flows for which the rotation rates ω and Ω were both positive (anti-clockwise) are summarised in Fig. 7. Each point shown in the (Ro, E) plane represents a separate experiment and the dominant wavenumber m in each region of parameter space is indicated by a number.

From Fig. 7 it is clear that no waves or instabilities occur in the upper left part of the regime diagram, where the basic zonal flow forced by the rotating ring is found to be stable. To the right of a critical line in this figure, however, given approximately by

$$Ro \approx 27E^{0.72 \pm 0.03}, \tag{9}$$

in the absence of a bottom slope (Früh and Read, 1999), wave-like meanders in the jet form and equilibrate to form polygonal patterns whose amplitude increases and whose wavenumber m tends to decrease with increasing Ro. In the absence of a β-effect, this form for the critical onset of instability corresponds approximately to a critical Reynolds number, $Re_c = UL/\nu$, where U is a typical azimuthal velocity scale representing the strength of differential rotation and L is the Stewartson layer thickness

$$L = \left(\frac{E}{4}\right)^{1/4} H. \tag{10}$$

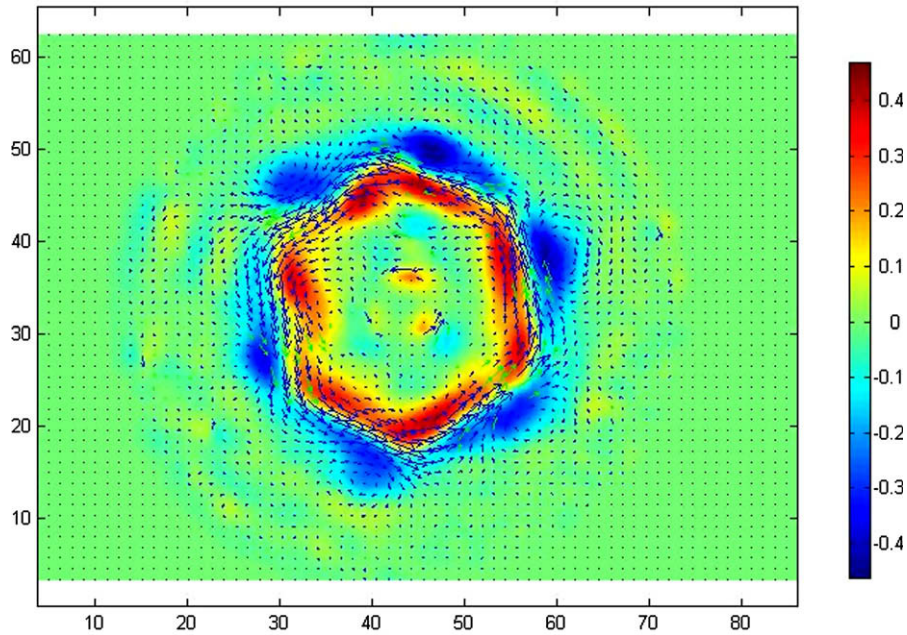In terms of E and Ro defined above, Re can be written as

Fig. 8. Instantaneous velocity field (arrows) and vorticity map (colour) of a hexagonal flow pattern observed in the *ring* (barotropic jet) laboratory experiment (see Fig. 4a) for $Ro = 7.4 \times 10^{-2}$, $E = 7 \times 10^{-5}$ and $\beta = 0$. Note how the flow is unstable to wave-like meanders with weak cyclones (anticyclones) inside (outside) the jet. The values in the centre of the image and outside of the circular black lines are not real (these regions are free of fluid) but consequence of interpolation of the data into a regular Cartesian grid.
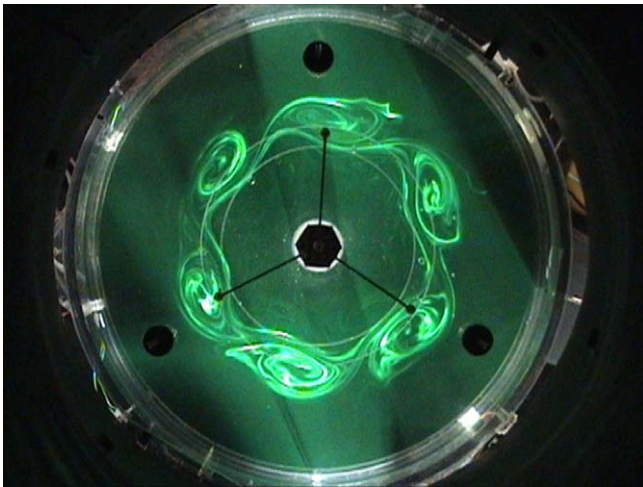

Fig. 9. Hexagonal pattern and associated barotropic vortices in the *ring* laboratory experiment (see Fig. 4a), for $Ro = 1.7 \times 10^{-1}$, $E = 2.5 \times 10^{-4}$ and $\beta = 9 \times 10^{-3} \, \text{cm}^{-1} \, \text{s}^{-1}$, visualised with fluorescein dye. The dye was injected through small needles on the bottom of the tank near the radius of the rotating ring.
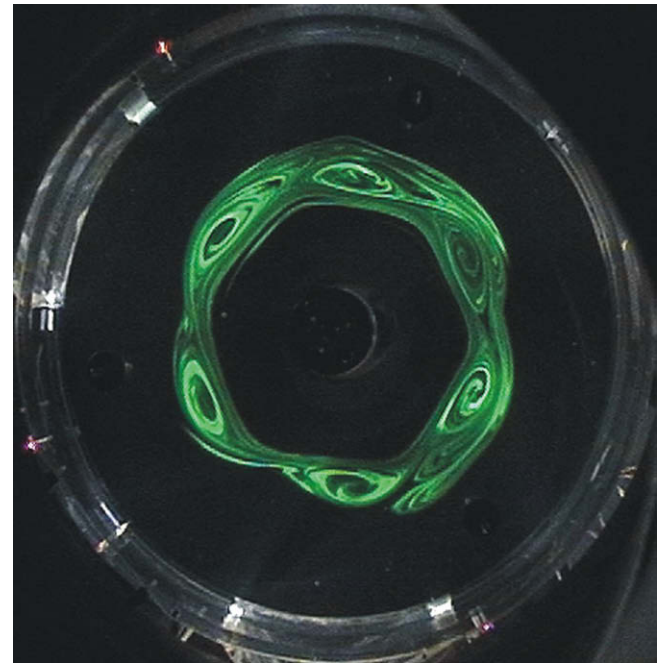
$$Re_c = \alpha Ro E^{-3/4}, \tag{11}$$

where α is a constant that depends on how U is defined relative to ω. We see, therefore, that the empirically determined relationship in Eq. (9) corresponds approximately to the Reynolds number in Eq. (11), with $Re_c \sim 37$ if $U = R\omega/4$ and α is taken to be $O(1)$.

The first onset of instability as the critical line is crossed is dominated by relatively weak eddies of fairly high wavenumber $m = 6$–8. The precise wavenumber that eventually dominated was found to vary somewhat between experiments across this range, though the flows would typically equilibrate to a pattern dominated by a single wavenumber. Transition boundaries to lower wavenumbers were found at larger values of Re though, as apparent in Fig. 7, the actual boundaries were not precisely determined by particular val-

Fig. 10. Hexagonal pattern and associated barotropic vortices in the *disks* laboratory experiment (see Figs. 4b and 5), for $Ro = 5 \times 10^{-2}$, $E = 8 \times 10^{-5}$ and $\beta = 3 \times 10^{-2} \, \text{cm}^{-1} \, \text{s}^{-1}$, visualised with fluorescein dye. The dye was injected through a small needle on the bottom of the tank at the split radius and the pattern remained stable (see corresponding movie in the online version).

ues of Re. At the highest values of Ro, $m = 2$ and 3 were found which, at the lowest values of E, were found to be time-dependent and apparently chaotic. In the present context, however, it is noteworthy that $m = 6$ flows occurred over a reasonably wide range of parameters for which $Ro < 0.1$. Moreover, the wavenumber observed was not uniquely determined by Ro and E but several different wavenumber flows could be found over similar parameter

ranges, depending mainly on the initial conditions. Such intransitivity and multiplicity of steady or quasi-periodic solutions is common in weakly nonlinear fluid systems.

The wavenumber selection in the presence of a barotropically unstable jet flow was also investigated to some extent by Niino and Misawa (1984), both experimentally and theoretically, based on a linear instability analysis. They noted from their linear instability analysis that the most rapidly growing wavenumber would depend on the jet radius R, measured by the non-dimensional parameter $\Gamma = R/L$, where L is the Stewartson layer thickness. When $\Gamma \gg 1$, the wavenumber of maximum growth then depended largely on Re_c, as found in our experiments. For the parameters applicable to our experiment, $\Gamma \sim 20$ so the curvature of the jet is not expected to play a major role. For $E = 10^{-4}$ and $Ro = 0.074$, the wavenumber of maximum growth rate is then predicted to lie around $m = 7.5$, close to the $m = 6$ observed.

4.2. Equilibrated m = 6 jet flows

Fig. 8 shows a quantitative velocity field from an equilibrated $m = 6$ flow with jet-like forcing at $Ro = 0.074$ and $E = 7 \times 10^{-5}$, corresponding to the profiles in Fig. 6. This field was derived by tracking the motion of groups of tracer particles in pairs of images, illuminated by a flat sheet of light around mid-level and separated in time by around 1 s. The velocity vectors are clearly dominated by the hexagonal meandering jet stream, with little indication of accompanying vortices. However, the latter are apparent in the field of relative vorticity in Fig. 8, where the exterior anticyclones are somewhat more prominent than the interior cyclones. These features are even more prominent in dye-streak visualisations of the flow, such as shown in Fig. 9, which illustrates a $m = 6$ flow in a nearby region of parameter space, within which fluorescein dye has been introduced both inside and outside the jet. Dye entrained into either cyclonic or anticyclonic closed vortices tends to remain trapped in each vortex, which then appears more prominently than the velocity field would indicate.

These wave patterns were found to equilibrate to steady amplitudes as the initial instability developed. The pattern then drifted slowly around the apparatus in the frame of the rotating table, in the same sense as ω but at a much slower rate. With a flat bottom in the tank, the waves were typically found to drift at velocities $\sim$9–15% of the ring forcing the jet flow. With a sloping bottom in the sense indicated in Fig. 4, emulating a positive but relatively weak β-effect, the wave pattern would tend to drift in a retrograde sense relative to the corresponding flat bottom case, somewhat slower in the reference frame of the tank and consistent with the Rossby wave dispersion relation (Pedlosky, 1987).

At the latitude of the hexagon in Saturn, the planetary β-effect is quite small and, according to present experiments, only weakly affects which wavenumber is observed. The only noticeable effect, in experiments with a β-effect was that the polygonal patterns looked sharper and more resilient than for the flat bottom case.

4.3. Comparison with other barotropic experiments

The formation of a robust and stable hexagonal structure in the presence of the jet flow discussed above presents a number of clear parallels with the North Polar Hexagon on Saturn. However, it is important to consider the robustness of the polygonal waves in the experiment to details of experimental geometry and flow structure.

The presence of equilibrated travelling waves from barotropic instability has been observed in a number of previous experiments. Sommeria et al. (1989), for example, produced barotropic jets using arrays of mass sources and sinks in a rotating, cylindrical container. They obtained various examples of polygonal wave features that equilibrated from an initial barotropic instability of the jet in their experiments, associated with a strong gradient of potential vorticity across the jet. The polygonal meanders in their experiments were accompanied by weak vortices on either side of the jet, much as found in our experiments though apparently somewhat weaker. Marcus and Lee (1998), however, argued that these vortices were essential to the stability and coherence of the polygonal wave pattern, owing to their tendency to lock in azimuthal phase through nonlinear interactions. They also drew attention to the importance of a sharp lateral PV gradient in the jets, which was interpreted as implying a significant barrier to radial mass transport.

Niino and Misawa (1984), Früh and Read (1999) and Aguiar (2008) investigated the barotropic instabilities of isolated, detached Stewartson shear layers, produced by differential rotation of disks flush with the upper and/or lower boundaries of a cylindrical tank (see Figs. 4b and 5). This led to a narrow, cylindrical vortex sheet at the edge of the differentially-rotating disk that could be barotropically unstable. Like the jet flows considered above, this could also lead to the formation of polygonal waves and vortices, though with some differences.

Fig. 10 shows an example of hexagonal shear layers obtained by Aguiar (2008) for $Ro = 5 \times 10^{-2}$, $E = 8 \times 10^{-5}$ and $\beta = 3 \times 10^{-2}$ cm^{-1} s^{-1}, in the same apparatus as the jet flows shown in Figs. 6–9 but using the disks configuration instead. This shows a dye streak image, in which fluorescein dye was injected into the vortex chain surrounding the flow co-rotating with the differentially-rotating disks. From this it is clear that the jet enclosing the chain of vortices acts as a transport barrier, since dye injected into the shear layer at the split radius remains trapped within the vortex chain and does not penetrate into the interior of the hexagon.

Both Früh and Read (1999) and Aguiar (2008) obtained regime diagrams for the detached shear layer configuration, covering similar ranges in Ro and E as in Fig. 7. Their results exhibited very similar features to those found in Fig. 7 for the jet flows, with a tendency for the initial supercritical flows to favour high wavenumbers with weak amplitudes. However, for more strongly supercritical flows, lower wavenumbers with stronger amplitudes were found, becoming time-dependent and chaotic at the largest values of Ro and Re_c. For a given value of forcing, the polygon observed was an intransitive meta-stable mode and, if the system is perturbed (e.g. by varying the differential rotation imposed – varying Ro), the pattern was often found to evolve into another polygonal shape of different wavenumber, depending on the strength of the perturbation. As with the jet flows, a number of the transitions between different modes showed some hysteresis and the system was often found to exhibit multiple solutions over regions of parameter space. Mode 6 is common among the spectrum of possibilities (ranging from $m = 1$–8, depending primarily on Ro) though is not unique in this regard as indicated by Fig. 7 (see also Früh and Read, 1999). Therefore, we see that the basic wavenumber selection mechanism is similar in both the shear layer and jet configurations. The detailed lateral structure of the barotropically unstable flow, however, clearly influences the relative prominence of jet meanders and associated vortices, and while Figs. 7 and 8 reveal a hexagonal sharp jet, Fig. 10 exhibits a broader hexagon that does not correspond to a jet.

5. Discussion

In this work, we have shown evidence that the North Polar Jet surrounding Saturn's North Pole is barotropically unstable, assuming baroclinic effects are comparatively weak, with a favoured wavenumber close to the $m = 6$ observed. Evidence from laboratory

experiments on fully developed barotropic instabilities demonstrate that such instabilities may equilibrate to form stable, coherent polygonal meanders that may be accompanied by closed, cyclonic and/or anticyclonic vortices on either side of the main meandering jet. The role and significance of these vortices remains somewhat controversial, however, and it remains to be proven whether they are crucial to the stability and coherence of the polygonal structures (as suggested by Marcus and Lee (1998)) or incidental. In the case of single shear layer flows such vortices form only on one side of the shear layer, which would tend to indicate that the locking mechanism invoked by Marcus and Lee (1998) is not essential to the formation of coherent, stable patterns. The trapping of fluid in vortices indicates the strongly nonlinear character of the equilibrated flow, whose stability and preferred lengthscale is ultimately determined more by vortex stability and transport optimisation arguments (Hollerbach et al., 2004; Polvani and Dritschel, 1993) than by linear perturbation theory. It is noteworthy that the vortices are more prominent in the dye visualisations than in the velocity field, which may explain why these features are not always easily identifiable in the observations of the hexagon.

The amplitude and form of the polygonal laboratory flows is evidently determined through nonlinear interactions with the zonal shear layer or jet, with a dynamic equilibrium being achieved between processes forcing the zonal flow and frictional processes dissipating the flow on different scales. In the case of the laboratory systems, the latter are clearly dominated by internal viscous diffusion. For Saturn, however, the origin of frictional processes is less clear, although it will presumably involve the action of small-scale turbulent mixing in a manner that has at least some parallels with laminar viscosity. This is one aspect of the suggested similarity of laboratory experiments with Saturn, however, that is more difficult to achieve in detail.

The selection of the dominant scale of the instability involves a number of factors, including the degree of supercriticality and the intrinsic lateral width of the unstable jet. Sommeria et al. (1991), for example, invoke the linear instability theory of Howard and Drazin (1964), which predicts a wavelength of maximum growth rate in inviscid barotropic instability of

$$\lambda_{max} = \pi L \sqrt{2}, \tag{12}$$

where L is now the lateral width of the jet. This worked reasonably well as a lower limit for the wavelength of the dominant fully-developed instabilities in their experiments, given their scaling estimate for L, with longer wavelength (lower wavenumber) flows. The more sophisticated theory of Niino and Misawa (1984), however, indicated that other factors will modify this simple result, including both the effect of jet curvature and internal viscosity. The discussion in Section 2 showed that a similar analysis for Saturn's North Polar Jet predicts a strong instability of relatively high wavenumber for a purely barotropic flow (infinite deformation radius), but that a finite deformation radius would reduce both the growth rate and favoured wavenumber of instability. Estimates of an appropriate deformation radius for Saturn (Sánchez-Lavega et al., 1996; Read et al., 2009b) suggest values of a few thousand km, which would be sufficient to reduce the wavenumber of maximum growth rate to $m < 8$, consistent with the observed hexagon.

Given that the Rayleigh–Kuo stability criterion is violated at a number of latitudes on Saturn, it is important to consider whether barotropic instabilities could be more widespread across the planet. It is of interest, for example, that the jet corresponding to the North Polar Jet in the southern hemisphere does not exhibit a stable hexagon feature, even though it appears to be of comparable strength to the northern jet. An application of the instability analysis of Section 2 to the southern jet as measured by Cassini indicates a weaker growth rate (under comparable conditions) that does not peak at finite wavenumbers, suggesting that the vorticity structure of the jet is simply less unstable there.

An instability analysis of the jet forming the so-called Ribbon Wave at 47°N (Godfrey, 1988; Sromovsky et al., 1983) also indicates the potential for barotropic instability as a possible mechanism. A good fit to measured values of the drift velocity for the Ribbon Wave was obtained by Polvani and Dritschel (1993) using a simple barotropic model of isolated vortices in spherical geometry.

A baroclinic origin for the Ribbon Wave has also been suggested by Godfrey and Moore (1986), although this relies on some unverified assumptions concerning the thermal and velocity structure below the clouds. Such an approach might also be able to account for the North Polar Hexagon, however. CIRS results (Fletcher et al., 2008), for example, do indicate some baroclinic character for both the hexagon and Ribbon Wave in the lower stratosphere, indicating that both features decay in amplitude above the tropopause. The true picture for both these phenomena may therefore ultimately entail a mixed baroclinic/barotropic origin. Observations of star-like stable $m = 6$ patterns have been reported in previous laboratory studies of baroclinic instability (Bastin and Read, 1997; Jacobs and Ivey, 1998), but the barotropic flows are more jet-like and exhibit polygonal patterns instead. Our experiments also suggest that the ephemeral polygonal waves and "pin-wheel" structures observed near the South Pole of Saturn by Cassini (Fletcher et al., 2008; Vasavada et al., 2006) can also be produced by barotropic instability, arising when the external forcing, i.e. strength or shape of the local jet, and consequently Ro varies. We recall that the experimentally observed modes are intransitive, and hence different patterns can be observed at similar points in parameter space, cf. similar latitudes in different hemispheres. Thus, even if jets at similar latitudes in the northern and southern hemispheres were more or less equally unstable under linear theory, this does not necessarily imply that similar patterns would equilibrate. The pattern selected may then depend on the past history of the flow, as well as its intrinsic potential for instability.

We conclude that the hexagonal structure and accompanying train of small vortices observed on Saturn can be plausibly interpreted as an equilibrated state of barotropic instability analogous to what is found in laboratory studies of similar instabilities. It appears that $m = 6$ is the preferred mode on Saturn in response to the strength and latitude of the jet, though this is not uniquely defined. It is not straightforward to make direct quantitative comparisons of parameter values for Saturn and laboratory experiments, because the depth and detailed vertical structure of the saturnian features are not known. Besides, given the large lengthscales in Saturn, the Reynolds number and the Ekman number are very large ($Re > 10^{12}$) and very small ($E < 10^{-14}$), respectively, and hence beyond comparison with the values for the laboratory flows. However, the experimental values of Ro around 0.03–0.1, found in our experiments to favour the formation of hexagonal waves, are plausible for Saturn. In addition, the experiments capture many qualitative features of the saturnian hexagon, including its morphology and stability.

Appendix A. Supplementary material

Supplementary data associated with this article can be found, in the online version, at doi:10.1016/j.icarus.2009.10.022.

References

Aguiar, A., 2008. Instabilities of a Shear Layer in a Barotropic Rotating Fluid. DPhil. Thesis, University of Oxford, Oxford, UK. 215pp.

Allison, M., Godfrey, D.A., Beebe, R.F., 1990. A wave dynamical interpretation of Saturn's Polar Hexagon. Science 247, 1061–1063.

Baines, K., Momary, T., Roos-Serote, M., Atreya, S., Brown, R., Buratti, B., Clark, R., Nicholson, P., 2007. Saturn's Polar Hexagon at depth: New images of stationary planetary waves in the North Polar Region by Cassini/VIMS. Geophys. Res. Abstr. 9, 02109.

Baines, K., Momary, T., Fletcher, L., Kim, J., Showman, A., Atreya, S., Brown, R., Buratti, B., Clark, R., Nicholson, P., 2009. Saturn's North Polar Region at depth: The North Polar Hexagon and North Polar Cyclone observed over two years by Cassini/VIMS. Geophys. Res. Abstr. 11, 3375.

Bastin, M.E., Read, P.L., 1997. A laboratory study of baroclinic waves and turbulence in an internally heated rotating fluid annulus with sloping endwalls. J. Fluid Mech. 339, 173–198.

Caldwell, J., Hua, X., Turgeon, B., Westphal, J.A., Barnet, C.D., 1993. The drift of Saturn's North Polar Spot observed by the Hubble Space Telescope. Science 206, 326–329.

Dowling, T.E., 1995. Estimate of Jupiter's deep zonal-wind profile from Shoemaker–Levy 9 data and Arnol'd's second stability criterion. Icarus 117 (2), 439–442.

Fincham, A.M., Spedding, G.R., 1997. Low cost, high resolution DPIV for measurement of turbulent fluid flow. Exp. Fluids 23, 449–462.

Fletcher, L.N., and 13 colleagues, 2008. Saturn's polar dynamics: Temperature and composition of the hotspots and hexagon. Science 319, 79–81.

Früh, W.-G., Read, P.L., 1999. Experiments on a barotropic rotating shear layer. Part 1. Instability and steady vortices. J. Fluid Mech. 383, 143–171.

Godfrey, D.A., 1988. A hexagonal feature around Saturn's North Pole. Icarus 76, 335–356.

Godfrey, D.A., 1990. The rotation period of Saturn's Polar Hexagon. Science 247, 1206–1208.

Godfrey, D.A., Moore, V., 1986. The saturnian ribbon feature – A baroclinically unstable model. Icarus 68, 313–343.

Gurnett, D.A., and 26 colleagues, 2005. Radio and plasma wave observations at Saturn from Cassini's approach and first orbit. Science 307, 1255–1259.

Hide, R., Titman, C.W., 1967. Detached shear layers in a rotating fluid. J. Fluid Mech. 29, 39–60.

Hollerbach, R., Futterer, B., More, T., Egbers, C., 2004. Instabilities of the Stewartson layer. Part 2. Supercritical mode transitions. Theor. Comp. Fluid Dyn. 18, 197–204.

Howard, L.N., Drazin, P.G., 1964. On instability of parallel flow of inviscid fluid in a rotating system with variable Coriolis parameter. J. Math. Phys. 43, 83–99.

Ingersoll, A.P., Beebe, R.F., Mitchell, J.L., Garneau, G.W., Yagi, G.M., Müller, J.-P., 1981. Interaction of eddies and mean zonal flow on Jupiter as inferred from Voyager 1 and 2 images. J. Geophys. Res. 86 (A10), 8733–8743.

Ingersoll, A.P., Dowling, T.E., Gierasch, P.J., Orton, G.S., Read, P.L., Sanchez-Lavega, A., Showman, A.P., Simon-Miller, A.A., Vasavada, A.R., 2004. Dynamics of Jupiter's atmosphere. In: Bagenal, F., Dowling, T.E., McKinnon, W.B. (Eds.), Jupiter: The Planet, Satellites and Magnetosphere. Cambridge University Press, Cambridge, UK, pp. 105–128.

Jacobs, P., Ivey, G.N., 1998. The influence of rotation on shelf convection. J. Fluid Mech. 369, 23–48.

Jansson, T.R.N., Haspang, M.P., Jensen, K.H., Hersen, P., Bohr, T., 2006. Polygons on a rotating fluid surface. Phys. Rev. Lett. 96, 174502-1–174502-4. doi:10.1103/PhysRevLett.96.174502.

van de Konijnenberg, J.A., Nielsen, A.H., Juul Rasmussen, J., Stenum, B., 1999. Shear-flow instability in a rotating fluid. J. Fluid Mech. 387, 177–204.

Kossin, J.P., Schubert, W.H., 2004. Mesovortices in Hurricane Isabel. Bull. Am. Meteorol. Soc. 85, 151–153.

Limaye, S.S., 1986. Jupiter: New estimates of the mean zonal flow at the cloud level. Icarus 65 (2–3), 335–352.

Limaye, S.S., Kossin, J.P., Rozoff, C., Piccioni, G., Titov, D.V., Markiewicz, W.J., 2009. Vortex circulation on Venus: Dynamical similarities with terrestrial hurricanes. Geophys. Res. Lett. 36, L04204. doi:10.1029/2008GL036093.

Marcus, P.S., Lee, C., 1998. A model for eastward and westward jets in laboratory experiments and planetary atmospheres. Phys. Fluids 10, 1474–1489.

Niino, H., Misawa, N., 1984. An experimental and theoretical study of barotropic instability. J. Atmos. Sci. 41, 1992–2011.

Pedlosky, J., 1987. Geophysical Fluid Dynamics. Springer-Verlag, Berlin, Heidelberg and New York.

Polvani, L.M., Dritschel, D.G., 1993. Wave and vortex dynamics on the surface of a sphere. J. Fluid Mech. 255, 35–64.

Read, P.L., Dowling, T.E., Schubert, G., 2009a. Saturn's rotation period from its atmospheric planetary-wave configuration. Nature 460, 608–610.

Read, P.L., Conrath, B.J., Fletcher, L.N., Gierasch, P.J., Simon-Miller, A.A., Zuchowski, L.C., 2009b. Mapping potential vorticity dynamics on Saturn: Zonal mean circulation from Cassini and Voyager data. Planet. Space Sci., in press. doi:10.1016/j.pss.2009.03.004.

Sánchez-Lavega, A., Lecacheux, J., Colas, F., Laques, P., 1993. Ground-based observations of Saturn's North Polar Spot and Hexagon. Science 260, 329–332.

Sánchez-Lavega, A., Lecacheux, J., Gomez, J.M., Colas, F., Laques, P., Noll, K., Gilmore, D., Miyazaki, I., Parker, D., 1996. Large-scale storms in Saturn's atmosphere during 1994. Science 271, 631–634.

Sánchez-Lavega, A., Rojas, J.F., Sada, P.V., 2000. Saturn's zonal winds at cloud level. Icarus 147, 405–420.

Schaeffer, N., Cardin, P., 2005. Quasigeostrophic model of the instabilities of the Stewartson layer in flat and depth-varying containers. Phys. Fluids 17, 104111-1–104111-12. doi:10.1063/1.2073547.

Sommeria, J., Meyers, S.D., Swinney, H.L., 1989. Laboratory model of a planetary eastward jet. Nature 337, 58–61.

Sommeria, J., Meyers, S.D., Swinney, H.L., 1991. Experiments on vortices and Rossby waves in eastward and westward jets. In: Osborne, A.R. (Ed.), Nonlinear Topics in Ocean Physics. North Holland, Amsterdam, pp. 227–269.

Sromovsky, L.A., Revercomb, H.E., Krauss, R.J., Suomi, V.E., 1983. Voyager 2 observations of Saturn's northern mid-latitude cloud features: Morphology, motions and evolution. J. Geophys. Res. 88, 8650–8666.

Vasavada, A.R., Hörst, S.M., Kennedy, M.R., Ingersoll, A.P., Porco, C.C., Del Genio, A.D., West, R.A., 2006. Cassini imaging of Saturn: Southern hemisphere winds and vortices. J. Geophys. Res. 111, E05004. doi:10.1029/2005JE002563.